ADVANCED ENERGY MATERIALS
www.advenergymat.de

A Versatile Sn-Substituted Argyrodite Sulfide Electrolyte for All-Solid-State Li Metal Batteries

*Feipeng Zhao, Jianwen Liang, Chuang Yu, Qian Sun, Xiaona Li, Keegan Adair, Changhong Wang, Yang Zhao, Shumin Zhang, Weihan Li, Sixu Deng, Ruying Li, Yining Huang, Huan Huang, Li Zhang, Shangqian Zhao, Shigang Lu, and Xueliang Sun**

Sulfide-based solid-state electrolytes (SSEs) for all-solid-state Li metal batteries (ASSLMBs) are attracting significant attention due to their high ionic conductivity, inherently soft properties, and decent mechanical strength. However, the poor incompatibility with Li metal and air sensitivity have hindered their application. Herein, the Sn (IV) substitution for P (V) in argyrodite sulfide Li_6PS_5I (LPSI) SSEs is reported, in the preparation of novel LPSI-*x*Sn SSEs (where *x* is the Sn substitution percentage). Appropriate aliovalent element substitutions with larger atomic radius ($R_{<Sn>} > R_{<P>}$) provides the optimized LPSI-20Sn electrolyte with a 125 times higher ionic conductivity compared to that of the LPSI electrolyte. The high ionic conductivity of LPSI-20Sn enables the rich I-containing electrolyte to serve as a stabilized interlayer against Li metal in sulfide-based ASSLMBs with outstanding cycling stability and rate capability. Most importantly, benefiting from the strong Sn–S bonding in Sn-substituted electrolytes, the LPSI-20Sn electrolyte shows excellent structural stability and improved air stability after exposure to O_2 and moisture. The versatile Sn substitution in argyrodite LPSI electrolytes is believed to provide a new and effective strategy to achieve Li metal-compatible and air-stable sulfide-based SSEs for large-scale applications.

1. Introduction

All-solid-state Li metal batteries (ASSLMBs) have been proposed to eliminate the safety problems and limited energy density (<500 Wh kg^{-1}) in current lithium-ion batteries (LIBs).[1] The solid-state electrolyte (SSE) is a critical component in ASSLMBs and has received extensive attention.[1a,2] Among the various types of SSEs, sulfide-based SSEs are considered as one of the most promising candidates, because of their high ionic conductivity, inherent softness for intimate contact between electrodes and electrolytes, as well as good mechanical strength for large-scale practical applications.[3]

However, two major detrimental factors have plagued the development of sulfide SSEs. First, the poor electrode material/sulfide SSEs interface deteriorates the battery performance.[2b,4] Since the compatibility issue between cathode materials and sulfide SSEs has prevented sulfide SSEs from achieving stable cycling performance, considerable efforts have been made to develop strategies to alleviate those problems.[1b,c,3b] In contrast, catastrophic Li metal anode interface makes the use of Li metal as an anode directly against sulfide electrolyte extremely challenging,[5] because of its strong reducing capabilities toward almost all kinds of sulfide SSEs, such as β-Li_3PS_4,[6] $Li_7P_3S_{11}$,[7] argyrodite-type,[8] and thio-LISICON-type electrolytes.[9] Moreover, the uneven Li deposition can cause Li dendrites formation, which can penetrate through the soft electrolyte to vitiate batteries.[10] Second, the air-sensitive nature of sulfide SSEs increases the difficulty for manufacturing and practical applications.[11] Due to the high oxygen affinity of P^{5+}, the sulfide SSEs that contain PS_4^{3-} structure blocks are extremely prone to reacting with H_2O to generate toxic H_2S gas. Thus, vacuum or inert gas atmosphere is required to handle sulfide SSEs, which would complicate the manufacturing and preparation processes with increased fabrication cost.

To alleviate the poor Li metal anode/sulfide SSEs interface problem, rich I or F-containing Li metal anode/sulfide SSEs

F. Zhao, Dr. J. Liang, Dr. C. Yu, Dr. Q. Sun, Dr. X. Li, K. Adair, C. Wang, Dr. Y. Zhao, S. Zhang, Dr. W. Li, Dr. S. Deng, R. Li. Prof. X. Sun
Department of Mechanical and Materials Engineering
University of Western Ontario
London, Ontario N6A 5B9, Canada
E-mail: xsun9@uwo.ca

Prof. Y. Huang
Department of Chemistry
University of Western Ontario
London, Ontario N6A 5B7, Canada

Dr. H. Huang
Glabat Solid-State Battery Inc.
700 Collip Circle, London, Ontario N6G 4X8, Canada

Dr. L. Zhang, Dr. S. Zhao, Dr. S. Lu
China Automotive Battery Research Institute Co., Ltd.
5th Floor, No. 43, Mining Building, North Sanhuan Middle Road
Haidian District, Beijing 100088, China

The ORCID identification number(s) for the author(s) of this article can be found under https://doi.org/10.1002/aenm.201903422.

DOI: 10.1002/aenm.201903422

 © 2020 WILEY-VCH Verlag GmbH & Co. KGaA, Weinheim

interfaces have been reported.[12] The functional interface can exhibit very stable electrochemical behaviors against sulfide SSEs in fabricated symmetric or full cells. LiI or LiF compositions in the solid-electrolyte-interphase (SEI) formed between Li metal and sulfide SSEs play crucial roles in preventing side reactions and Li dendrites formation. Especially when I- or F-based sulfide SSEs are used, high current density and reversible cut-off capacities can be achieved to meet the requirement of high-energy-density ASSLMBs.[12d,13] Nevertheless, it is still very challenging to realize air-stable sulfide SSEs with decent room temperature (RT) ionic conductivity (>10^{-4} S cm^{-1}). Li–Sn–S electrolytes (Li_4SnS_4 and Li_2SnS_3) were demonstrated to possess excellent air stability, benefiting from the hard-softs-acids-bases (HSAB) theory.[14] Sn is classified as a soft acid, which prefers to bond with soft base S rather than hard base O. However, the low ionic conductivity of pristine Li–Sn–S electrolytes limited at 10^{-5} S cm^{-1} level restrains their development. Although As substitution in Li_4SnS_4 can improve the RT ionic conductivity to reach 1.0×10^{-3} S cm^{-1}, the highly toxic As element brings additional safety and environmental concerns.[15] Nevertheless, the air stability of the sulfide electrolytes is predicted to be improved after Sn substitution in the PS_4^{3-} structure. Furthermore, the aliovalent element (Sn) substitution with larger atomic radius and lower valence compared with phosphorus (P) can expand the cell volume and increase the Li solubility in the unit cells, which can synergistically increase the corresponding ionic conductivity.[16]

Argyrodite electrolytes Li_6PS_5X (LPSX, X = Cl, Br, and I) represent one type of popular sulfide electrolytes, due to the low cost of raw materials and high ionic conductivity.[17] Both LPSCl and LPSBr with a high ionic conductivity of >1×10^{-3} S cm^{-1} still suffer from the problems that are mentioned above.[8,18] Li_6PS_5I (LPSI) has received less attention, because the low S^-/I^- exchange disorder leads to a low conductivity in the order of 10^{-6} S cm^{-1}.[19] However, the high I concentration in the electrolyte itself is highly anticipated to stabilize the Li metal/LPSI-based electrolyte interface in ASSLMBs if decent ionic conductivity can be obtained. Recent studies show that the ionic conductivity of LPSI SSE can be significantly improved by aliovalent element substitutions.[16a,20] Different from previous work that is fundamentally dedicated to improve the ionic conductivity fundamentally, we aim in using a versatile strategy to achieve an excellent sulfide SSE with good Li metal compatibility, improved air stability, and decent ionic conductivity, simultaneously. Herein, we originally propose to partially substitute Sn for P in LPSI argyrodite electrolytes to prepare new argyrodite-type electrolytes: LPSI-xSn or $Li_{6+\gamma}P_{1-\gamma}Sn_\gamma S_5I$ (x is the Sn substitution percentage, $\gamma = x$%). The optimized ionic conductivity of LPSI-20Sn reaches a value as high as 3.5×10^{-4} S cm^{-1}, which is 125 times higher than that of the LPSI electrolyte without Sn substitution. More importantly, LPSI-20Sn electrolyte is stable without any degradation in pure O_2, and even shows negligible decrease in ionic conductivity after being exposed to 10% humidity atmosphere and postheating treatment. Additionally, the robust Li/LPSI-20Sn interface enables ultrastable Li plating/stripping for over 200 h at a high current density (1.26 mA cm^{-2}) and cut-off capacity (1 mAh cm^{-2}) in Li//LPSI-20Sn//Li symmetric cells. The application of this electrolyte is also demonstrated in ASSLMBs by using LPSI-20Sn as the Li anode interlayer in full cells that exhibits excellent cycling stability and rate capability.

2. Results and Discussion

2.1. Synthesis and Structure of LPSI-xSn SSEs

Conventional solid-state-reaction methods were employed to synthesize a series of Sn-substituted argyrodite LPSI-based electrolytes with various Sn substitution percentages: LPSI-xSn (x = 0, 10, 20, 30, 50, 80, and 100, where x = 0 is the pristine LPSI electrolyte, and x = 100 means complete substitution of P with Sn in the LPSI electrolyte). The corresponding chemical reaction equation can be written as: $(5 + \gamma)\ Li_2S + (1 - \gamma)\ P_2S_5 + (2\gamma)\ SnS_2 + 2\ LiI = 2\ Li_{6+\gamma}P_{1-\gamma}Sn_\gamma S_5I$, where γ is the substitution content of Sn ($0 \le \gamma \le 1$). X-ray diffraction (XRD) measurements were first carried out to study the phase composition of the prepared LPSI-xSn electrolytes. As shown in **Figure 1**a, pure LPSI phase can be obtained without any Sn substitution, which is highly consistent with the referenced LPSI (PDF# 04-018-1431). The border diffraction peak at around 18° is assigned to the Kapton tape, which is used to seal the XRD sample and prevent air exposure. With the Sn substitution percentage increasing, the characteristic diffraction peaks of LPSI vanish, while some peaks belonging to the Li_4SnS_4 and LiI phases raise gradually. Close inspection on the XRD pattern in the 2θ range of 24.5°–25° (Figure 1b) suggests that the strongest diffraction peak in LPSI patterns at 24.8° shifts continually to lower diffraction angle along with increased Sn substitution amount. Figure 1c presents a low-speed-scan XRD with Rietveld refinement of the representative LPSI-20Sn electrolyte. One predominant phase is an argyrodite structure with cubic symmetry (space group F-43m) with unit cell parameters: $a = b = c$ = 10.21760 Å, $\alpha = \beta = \gamma$ = 90.00°, and V = 1066.71 $Å^3$ (Table S1, Supporting Information). The small amount of impurity (2.7%) is identified as LiI. The distorted argyrodite structure (as shown in Figure 1d) exhibits a nonstoichiometric composition of $Li_{6.24}P_{0.823}Sn_{0.177}S_{4.58}I_{0.9}$ with Li-rich and vacancy in the structure (Table S2, Supporting Information). The substituted Sn atom in the 4b site is shared with P and the occupation is around 17.8%, which is close to the designed substitution content (20%). It is found that the Li-rich environment and vacancy distribution within the synthesized of $Li_{6.24}P_{0.823}Sn_{0.177}S_{4.58}I_{0.9}$ is quite different from that of the Li_6PS_5I structure (Table S3, Supporting Information), indicating different Li^+ conduction and migration pathways in the electrolytes. The enlarged crystal unit cell is derived from the replacement of P with Sn, which has a larger atomic radius ($R_{<Sn>}$ 1.40 Å > $R_{<P>}$ 1.10 Å), and the increased Li^+ ion concentration in the specific unit cell. The characteristic unit cell is expected to benefit the Li^+ ion conduction and to increase the ionic conductivity.[16] A similar phenomenon is observed in the LPSBr-xSn (x = 0, 1, 5, 10, 12.5, 15, 20, 30) system (Figure S1, Supporting Information), but cannot occur in the LPSCl-xSn (x = 0 and 30) system (Figure S2, Supporting Information). The reason is related to the atomic radius of X in the argyrodite structure (X = Cl, Br, and I), where the larger size of the I atom endows the LPSX structure with more possibilities of various aliovalent elemental substitutions.[16a]

© 2020 WILEY-VCH Verlag GmbH & Co. KGaA, Weinheim

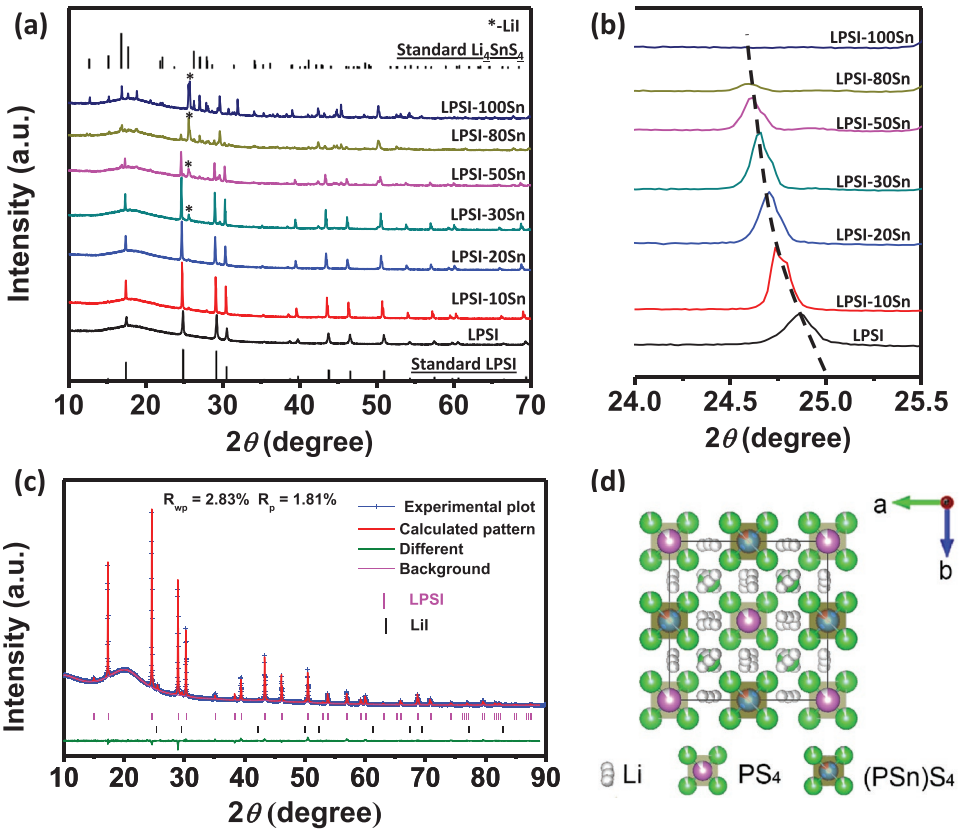

Figure 1. a) XRD patterns of the prepared LPSI-*x*Sn sulfide-based electrolytes ($x = 0, 10, 20, 30, 50, 80, 100$). b) Magnified region of the XRD patterns in the 2θ range: $24° < 2\theta < 25.5°$. c) Low-speed-scan XRD pattern of representative LPSI-20Sn electrolyte and the corresponding Rietveld refinements. d) Structure of the prepared LPSI-20Sn ($Li_{6.24}P_{0.823}Sn_{0.177}S_{4.58}I_{0.9}$) from the view of perpendicular to *c*-axis.

Furthermore, Raman spectral measurements were conducted to verify Sn substitution in the position of P in LPSI-*x*Sn electrolytes. As shown in Figure S3 in the Supporting Information, the Raman shift at 416.3 cm^{-1} is the fingerprint position that reflects the PS_4 blocks (P only exists in tetrahedral PS_4 in LPSI electrolyte) in LPSI electrolyte.[21] After Sn substitution, the intensity of PS_4 peak reduces, and an additional peak in the 337.7–342.9 cm^{-1} region appears and increases in intensity with increased Sn substitution percentage. Co-existence of the two peaks implies the formation of $(P/Sn)S_4$ structure. In the fully Sn-substituted sample LPSI-100Sn, the only characteristic peak at 342.9 cm^{-1} agrees well with the previously reported position that indicates the formation of SnS_4 structure.[14c] Scanning electron microscopy (SEM) was used to examine the morphology and the element distribution in LPSI-20Sn electrolyte (Figure S4, Supporting Information). Microsized irregular LPSI-20Sn secondary particle is composed of nanosized primary particles (≈100 nm). Energy dispersive spectroscopy (EDS) element mapping for the selected area demonstrates that P, S, Sn, and I are homogeneously dispersed in granular LPSI-20Sn electrolytes. In other words, the Sn precursors can fully mix and react with other raw materials for substitution. The results of the above mentioned structural and compositional analyses confirm that successful Sn substitution for P in LPSI-*x*Sn structure is achieved. The expanded unit cells and small electrolyte particle sizes are desirable for high ionic conductivity and applicable LPSI-based electrolytes. The derived I chemistry at Li/electrolyte interface is favorable toward achieving a stable Li metal anode. In addition, the formation of the Sn—S bonds is also beneficial for enhanced air stability.

2.2. Ionic Conductivity and Li^+ Ion Dynamics of LPSI-*x*Sn SSEs

Electrochemical impedance spectroscopy (EIS) was measured to deduce the ionic conductivity (σ) of the prepared LPSI-*x*Sn electrolytes. The plot of σ value as a function of Sn content at RT is shown in **Figure 2**a. The LPSI electrolyte without any Sn substitution shows a very low σ of 2.8×10^{-6} S cm^{-1}, which is in agreement with previously reported literatures.[19] After partly replacing P with Sn in the tetrahedral PS_4 of LPSI-based electrolyte, dramatic change of σ takes place. 10% Sn substitution can significantly increase the σ to 4.2×10^{-5} S cm^{-1}, showing a 15 times increase. The optimized σ can reach 3.5×10^{-4} S cm^{-1} when the Sn substitution percentage is 20%. Compared with the σ of the pristine LPSI electrolyte, the σ of LPSI-20Sn exhibits an increase of 125 times. This makes LPSI-20Sn comparable to some common sulfide SSEs in terms of ionic conductivity.[2a] Nevertheless, too much Sn substitution can lead to decrease in σ as a result of the formation of impurity phases. Figure 2b compares the Arrhenius plots of LPSI and LPSI-20Sn electrolytes derived from a series of

© 2020 WILEY-VCH Verlag GmbH & Co. KGaA, Weinheim

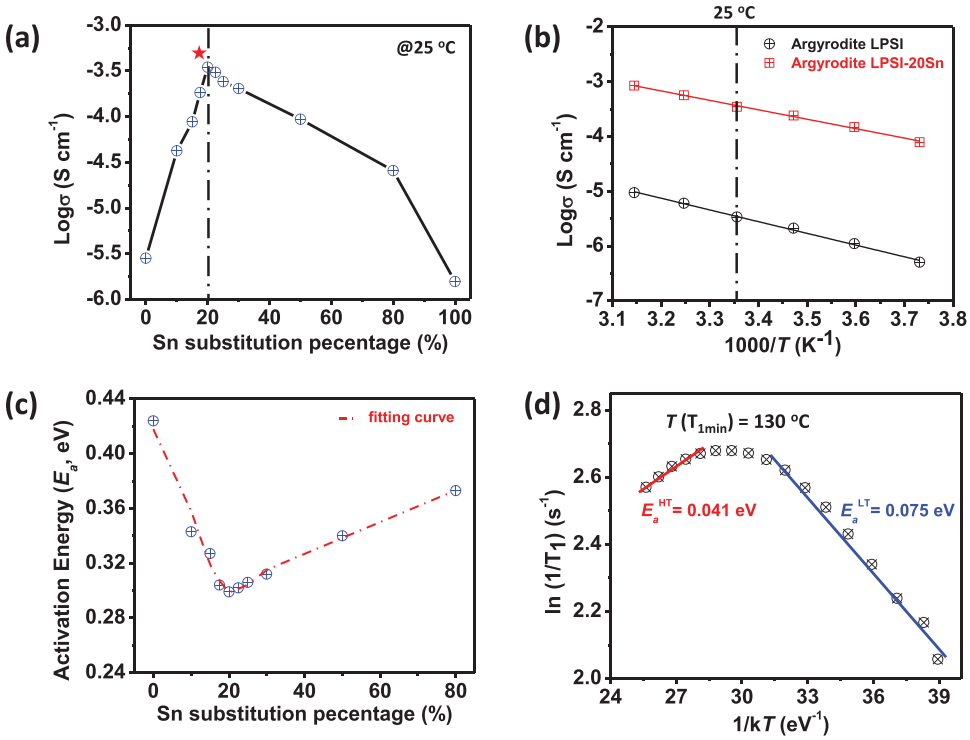

Figure 2. a) The room temperature (RT, 25 °C) ionic conductivity of LPSI-*x*Sn sulfide-based electrolytes with different amounts of Sn substitution ($x = 0$, 10, 15, 17.5, 20, 22.5, 25, 30, 50, 80, 100). b) Arrhenius plots of the LPSI-20Sn electrolyte and LPSI electrolyte without Sn substitution. c) Change trend of the activation energy against different substitution percentages. d) Temperature-dependent ^{7}Li spin–lattice relaxation (SLR) NMR rates measured in the laboratory frame for LPSI-20Sn electrolytes.

ionic conductivities in a temperature range from −5 to 45 °C (interval 10 °C for each point). The σ value of the LPSI-20Sn electrolyte at any given temperature is about two orders of magnitude higher than that of LPSI electrolyte without Sn substitution. Furthermore, the activation energy of Li^+ ion transport in LPSI-20Sn structure (E_a-LPSI-20Sn) calculated from the slop of Arrhenius plot is 0.299 eV, which is much lower than that in LPSI structure (E_a-LPSI = 0.424 eV). Arrhenius plots of other Sn-substituted LPSI-*x*Sn electrolytes ($x = 10$, 15, 17.5, 22.5, 25, 30, 50, 80) are also presented in Figure S5 in the Supporting Information, and the derived activation energy of each composition is displayed in Figure 2c. The trend for change in E_a against Sn substitution amount is inverse compared with the trend in Figure 2a. Li^+ ion movement becomes much easier after Sn substitution in the LPSI structure. The lowest point appears with a substitution percentage of 20%, which is corresponding to the fastest Li^+ ion motion and the largest ionic conductivity in this structure. The activation energy shows an increasing trend after the Sn substitution percentage is over 20%. This is ascribed to the gradually increasing amount of impurity phases (mainly LiI and Li_4SnS_4). σ of another Sn-substituted system, LPSBr-*x*Sn (substitution percentage $x = 1$, 2.5, 5, 10, 12.5, 15, 20, 30), was also investigated to further understand the Sn substitution effect on the ionic conductivity. The results are shown in Figure S6 in the Supporting Information. The optimized σ value of 2.1×10^{-3} S cm^{-1} is achieved when the degree of Sn substitution is at 12.5% in the LPSBr structure. This σ value of LPSBr-12.5Sn is twice larger than that of LPSBr electrolyte (σ-LPSBr = 1.0×10^{-3} S cm^{-1}). Meanwhile, the activation energy of LPSBr-12.5Sn (0.30 eV) is lower than that of LPSBr (0.33 eV).

^{7}Li solid-state nuclear magnetic resonance (^{7}Li-NMR) was employed to probe the Li^+ ion dynamics in LPSI-20Sn at an atomic level. It can provide information on bulk ionic conductivity of the electrolyte without the contribution from grain boundaries in SSEs. First, the line-shapes of ^{7}Li static NMR resonance of LPSI-20Sn at different temperatures are presented as Figure S7 in the Supporting Information. The line-shape of ^{7}Li resonance becomes narrower with increasing temperature, a phenomenon reported elsewhere.[22] The observed line narrowing is due to the increased Li-ion mobility that averages out the dipolar interaction at higher test temperatures. Then, ^{7}Li spin–lattice relaxation (SLR) rates ($1/T_1$) were measured as a function of temperature (T). As shown in Figure 2d, a minimum T_1 (T_{1min}) is observed when T reaches 130 °C. The slopes of the linear portions of the curves on both low temperature (LT) and high temperature (HT) sides of the T_{1min} are used to calculate the activation energy of short-range (E_a^{LT}) and long-range (E_a^{HT}) Li^+ ion mobility, respectively.[23] They are 0.041 and 0.075 eV for E_a^{HT} and E_a^{LT}, respectively. These results are reasonable as they are much lower than the values derived from the EIS measurements, because the negative effect of boundary has been excluded.[22,23] In contrast, for the LPSI electrolyte without Sn substitution, the ^{7}Li SLR results (Figure S8, Supporting Information) show a larger activation energy in both HT and LT regions (0.076 and 0.082 eV, respectively). All above Li^+ ion motion analyses (both EIS and ^{7}Li-NMR results) confirm that replacing P with appropriate amounts of Sn can

© 2020 WILEY-VCH Verlag GmbH & Co. KGaA, Weinheim

promote Li^+ ion transport in the favorable Sn-substituted argyrodite LPSI structures. The Sn substitution results in significantly improved ionic conductivity and reduced Li^+ ion motional activation energy.

2.3. Air Stability of LPSI-20Sn SSEs

After optimizing ionic conductivity and probing Li^+ ion mobility in the LPSI-*x*Sn electrolyte system, the air stability of the LPSI-20Sn electrolyte was examined. The reactivity toward O_2 was investigated by monitoring the weight change of the electrolyte in a microbalance of a thermogravimetric analysis (TGA) instrument when the electrolyte is exposed to pure O_2 (99.999%) flow. **Figure 3**a illustrates the change in mass percentage of the electrolytes as a function of the exposure time in pure O_2 atmosphere. Compared with pure LPSI electrolyte (specific surface area: 1.50 $cm^2\ g^{-1}$) whose weight increases by 1.12% after being exposed to O_2 for 10 h, LPSI-20Sn electrolyte (specific surface area: 1.41 $cm^2\ g^{-1}$) shows significantly improved resistance toward O_2. The mass percentage increase is as low as 0.28% after exposure to pure O_2 for 10 h and only 0.35% after 20 h, which indicates that the LPSI-20Sn electrolyte maintains its structure in pure O_2 after initial minor decomposition. In addition to the good resistance to O_2, LPSI-20Sn electrolyte also exhibits excellent stability toward moisture. As shown in Figure 3b, the XRD patterns exhibit little difference between LPSI-20Sn electrolytes before and after exposure to 10% humidity overnight except for some small unknown impurity peaks (Figure S9, Supporting Information). X-ray absorption near-edge spectra (XANES) of P K-edge (Figure 3c) cannot also witness the chemical environment change of P after exposing to 10% humidity overnight, but the ionic conductivity of LPSI-20Sn drops slightly to 2.2×10^{-4} S cm^{-1} at RT (Figure 3d). This might be ascribed to the decomposition of some PS_4 blocks which are not effectively Sn substituted. However, the ionic conductivity of LPSI-20Sn can recover to 3.1×10^{-4} S cm^{-1} at RT after a postheating process (180 °C in vacuum oven) is conducted. The XRD pattern of the postheated sample in Figure 3b confirms that the impurity phases vanish and all featured diffraction peaks agree well with the pristine LPSI-20Sn electrolyte. In contrast, a larger amount of impurity diffraction peaks can be observed after exposing LPSI electrolytes to 10% humidity (Figure S10, Supporting Information). Even after the same postheating treatment, the diffraction peaks from impurities still exist.

Density functional theory (DFT) calculations of the oxygen replacement reaction energy (ΔE) were conducted to reveal the improved air stability of LPSI-20Sn electrolytes. Generally, the first-step degradation of the sulfide electrolyte containing PS_4 tetrahedron toward O_2 or H_2O is related to the replacement reaction of S with O atom.[11] The oxygen replacement reaction energy of LPSI-20Sn and LPSI electrolytes was simulated based on the differential energy by changing one of the S atoms to O atom in the model structure. When changing one of the PS_4 tetrahedrons to PS_3O tetrahedron in the whole crystal structure, the reaction can be simulated as PS_4 tetrahedron + O atom = PS_3O tetrahedron + S atom. Therefore, the oxygen replacement reaction energy (ΔE) can be calculated as $\Delta E = U_{(\text{S atom})} + U_{(\text{PS3O tetrahedron})} - U_{(\text{O atom})} - U_{(\text{PS4 tetrahedron})}$. The oxygen replacement reaction energy (ΔE) can be defined as one of the indicators to evaluate the reaction capabilities between

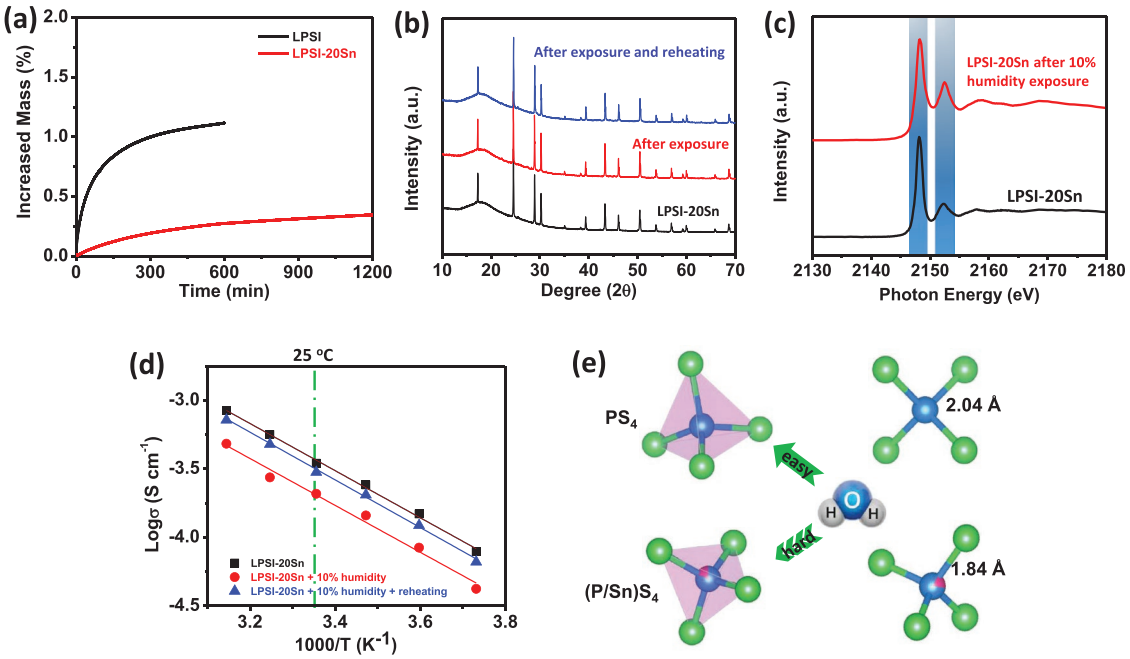

Figure 3. a) Time-resolved mass change of LPSI and LPSI-20Sn electrolytes in pure O_2. b) XRD patterns and d) Arrhenius plots of the LPSI-20Sn electrolyte before and after exposure to air with 10% humidity, as well as after postheating process. c) XANES of P K-edge in LPSI-20Sn and the sample after exposing to 10% humidity. e) Schematic diagram of the difficult degree of being oxidized by H_2O of PS_4 and $(P/Sn)S_4$ tetrahedrons based on the DFT calculation.

© 2020 WILEY-VCH Verlag GmbH & Co. KGaA, Weinheim

sulfide electrolytes and O_2 or H_2O. As a result of the DFT calculation, the ΔE of LPSI and LPSI-20Sn electrolyte is 2.667 and 9.298 eV, respectively. The results indicate a much stronger bonding energy of (P/Sn)–S in the $(P/Sn)S_4$ tetrahedron than that of P–S in the PS_4 tetrahedron when replacing S with O. In other words, a better resistance capability of LPSI-based electrolytes can be obtained after Sn substitution (see the schematic diagram in Figure 3e). The Sn substituted in the lattice prefers to bond to S rather than O, endowing the LPSI-20Sn electrolyte to have a stable crystal structure.

2.4. Li Metal Compatibility of LPSI-20Sn SSEs

The Li anode interface stability of Li/LPSI-20Sn compared to that of Li/LPSI was evaluated by cycling the Li–Li symmetric cells. The results are shown in **Figure 4**. Under a current density of 0.1 mA cm^{-2} and a cut-off capacity of 0.1 mAh cm^{-2}, Li//LPSI-20Sn//Li symmetric cell can perform an ultrastable Li plating/stripping for over 700 h (350 cycles) at RT (Figure 4a). Even under a high current density of 1.26 mA cm^{-2} and cut-off capacity of 1 mAh cm^{-2}, our Li//LPSI-20Sn//Li symmetric cell can still display a very stable Li plating and stripping behavior for ≈200 h (125 cycles) at RT (Figure 4c). The durability can be comparable to the best performances in the previous reported symmetric cells using sulfide-based electrolytes (Table S4, Supporting Information). Detailed plating/stripping voltage profiles under low current density of 0.1 mA cm^{-2} can be seen in the magnified regions at different cycling time points in Figure 4a-1–a-3. Flat and axisymmetric polarization curves exhibit ultrastable and highly reversible Li plating and stripping behaviors at the Li/LPSI-20Sn interface. The initial overpotential is 30 mV, which is comparable to that of the LiI-doped LPS electrolytes.[12d] After 700 h of stable Li plating and stripping process, the overpotential increases to 56 mV, which is due to the in situ formed SEI layer slightly increasing the interfacial impedance. In sharp contrast, the Li–Li symmetric cell using LPSI as the electrolyte even cannot plate and strip regularly for one cycle. The ultralow ionic conductivity of LPSI leads to a high overpotential of more than 3 V. The violent

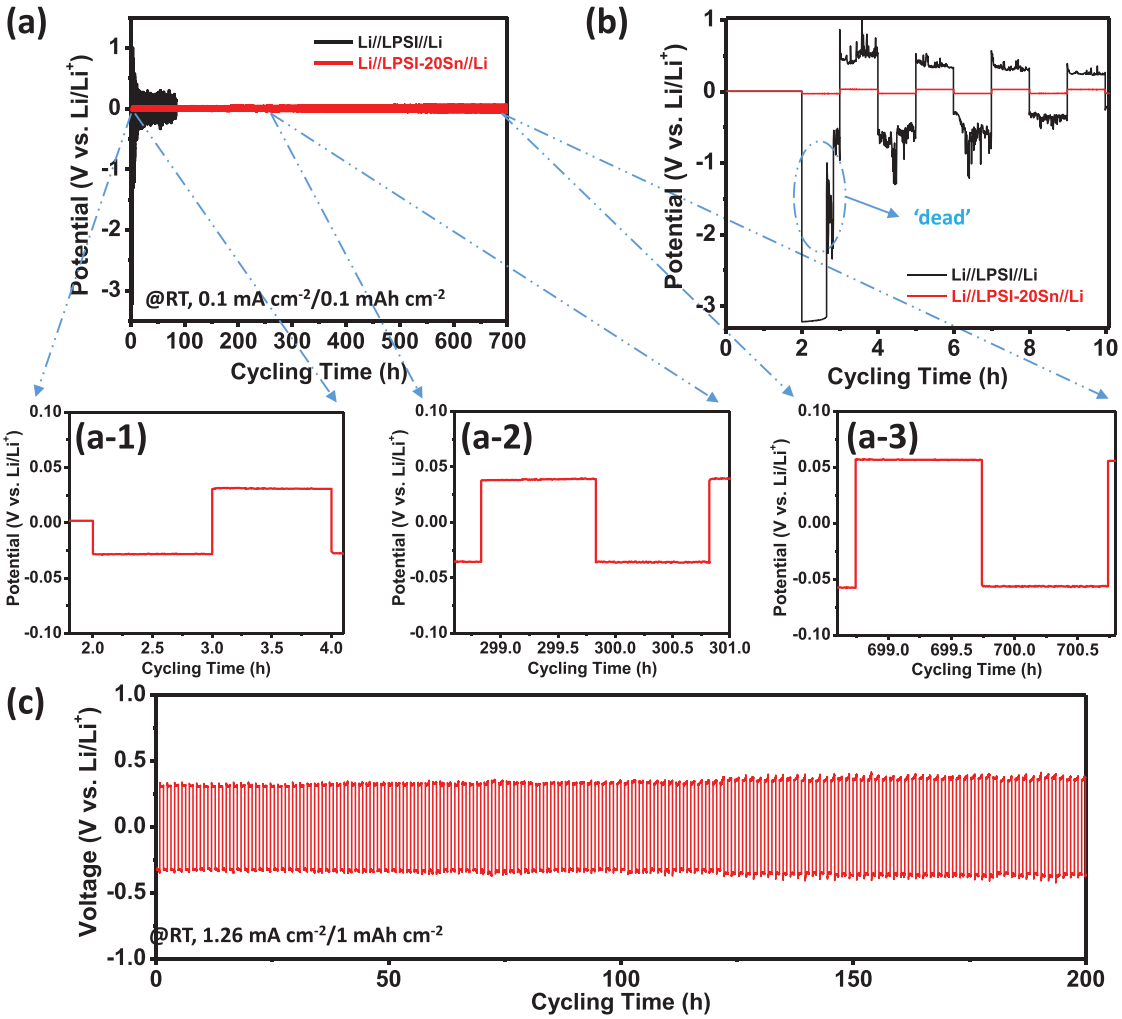

Figure 4. Li–Li symmetric cells performance: a) comparison of using LPSI and LPSI-20Sn to operate symmetric cells; b) magnified region of 0–10 h in (a); a-1–a-3) The magnified regions of the voltage profile at different time from (a). c) Li plating/stripping polarization of the Li//LPSI-20Sn//Li symmetric cell tested under 1.26 mA cm^{-2}/1 mAh cm^{-2}.

© 2020 WILEY-VCH Verlag GmbH & Co. KGaA, Weinheim

fluctuation and gradually reduced overpotential indicate poor Li plating/stripping kinetics at the Li/LPSI interface (Figure 4b). Time-resolved EIS of the Li//LPSI-20Sn//Li symmetric cell was also used to enclose the stable Li/LPSI-20Sn interface before symmetric cell cycling (Figure S11, Supporting Information). During the 24 h after assembling, negligible impedance change can be found in the Li//LPSI-20Sn//Li symmetric cell. This reveals that there is no side reaction happening to the Li/LPSI-20Sn interface. The robust Li anode interface benefits from the rich I-containing electrolytes (7.7% mole ratio), which has also been demonstrated in LiI-doped LPS electrolytes. SEM measurements for the Li metal surface were conducted after Li plating/stripping in the Li//LPSI-20Sn//Li symmetric cell at 0.1 mA cm^{-2}/0.1 mAh cm^{-2} for ≈60 h (Figure S12, Supporting Information). A relatively smooth and dense Li surface is formed in situ, which shows a uniform distribution of I-containing species. X-ray photoelectron spectroscopy (XPS) measurements for the surface further confirm that the I species is LiI compounds (Figure S13, Supporting Information). The binding energy of $3d_{2/3}$ (630.6 eV) and $3d_{5/3}$ (619.1 eV) agree well with the previous literature.[24] The LiI formed at the Li anode interface can serve as a vital component for stabilizing SEI to create uniform electron and ion distribution as well as suppress the formation of Li dendrites.[12b,25]

2.5. Full Battery Performance

To demonstrate the applicability of the LPSI-20Sn electrolyte in ASSLMBs, we further employed the LPSI-20Sn electrolyte as the interlayer separating the Li metal and $Li_{10}GeP_2S_{12}$ (LGPS) electrolyte, with the use of a $LiNbO_x$ coated $LiCoO_2$ (LCO@LNO) cathode (as shown in the schematic diagram **Figure 5**a). RT galvanostatic charge–discharge tests were conducted on full batteries in a voltage window of 2.8–4.2 V (Li/Li^+, the same below) and under various current densities at RT. Figure 5b shows the first three charging and discharging curves under a low current density of 0.05 C (1 C = 140 mA g_{LCO}^{-1}). The charge and discharge curves with a plateau at ≈3.9 V are extremely similar to those in the liquid electrolyte systems, suggesting highly reversible Li^+ ion de-intercalation and intercalation behavior toward the LCO cathode materials.[26] The first-cycle reversible specific capacity is 123.7 mAh g^{-1}, and the corresponding Coulombic efficiency can reach as high as 91%. The first cycle efficiency is one of the highest reported for ASSLMBs using Li metal as the anode directly. The high efficiency is attributed to the excellent stability of Li/LPSI-20Sn interface. Because Li^+ ions can smoothly shutter through this LiI-assistant robust Li anode interface, no waste of Li source accounts for consumption of irreversible reactions and the Li dendrites. After three initial cycles at 0.05 C, the cycling stability of this full battery at 0.1 C at RT is displayed in Figure 5c. The reversible specific capacity maintains steady at ≈113.0 mAh g^{-1}, and negligible capacity decay is observed in the first 20 cycles. After 50 cycles, a capacity retention of 88.5% can be achieved. Remarkably, the average coulombic efficiency reaches 99.8% during the long cycling process, suggesting highly reversible Li^+ ion intercalation/de-intercalation. In sharp contrast, the full battery without the LPSI-20Sn functional interlayer (Li//LGPS//LCO@LNO//LGPS) shows large voltage polarization at 0.05 C and even cannot deliver reversible capacity at 0.1 C (Figure S14, Supporting Information). Apart from the cycling stability, the rate capability was also evaluated as shown in Figure 5d. The rate performance was obtained by elevating the discharge current densities, while keeping the charge current density at 0.05 C. This method enables the complete uptake of Li source

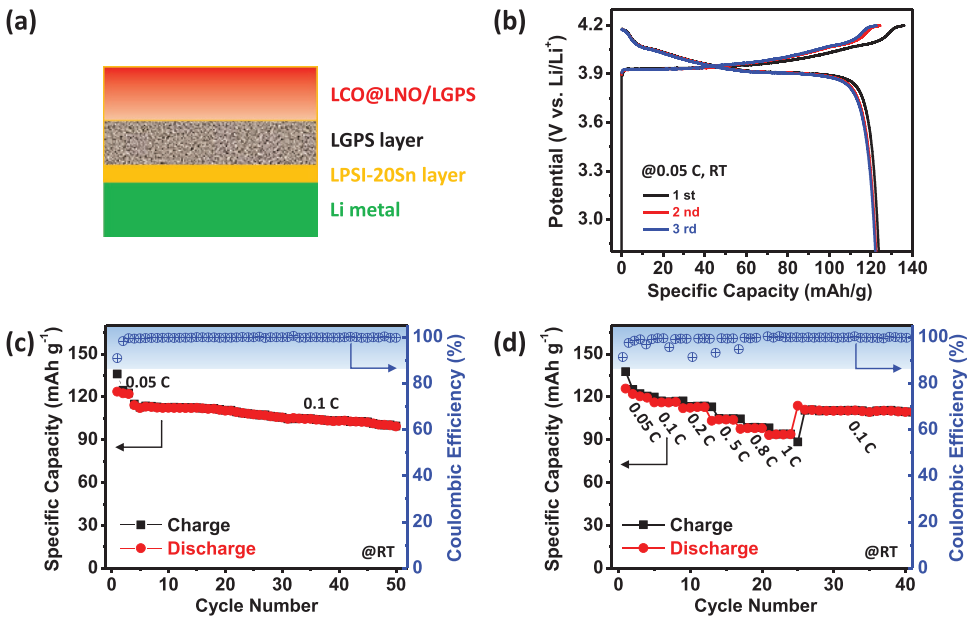

Figure 5. Electrochemical performance of ASSLMBs: a) schematic diagram of the Li/LPSI-20Sn//LGPS//LCO@LNO//LGPS ASSLMBs with the highlighted anode interlayer; b) the first three charge–discharge profiles of the fabricated ASSLMBs; c) cycling stability and d) rate capability of the Li/LPSI-20Sn//LGPS//LCO@LNO//LGPS at RT.

© 2020 WILEY-VCH Verlag GmbH & Co. KGaA, Weinheim

from the cathode and an estimate of the influence of sluggish Li^+ ion transport problem in cathode composites.[27] In this way, reversible specific capacities can hold to as high as 98.1 and 93.8 mAh g^{-1} at high current densities of 0.8 and 1 C, respectively. Moreover, when the current density is reduced to 0.1 C afterward, the specific capacity can recover to 111.0 mAh g^{-1} and remains stable in the following cycling. Unlike the reported results that indicate Li dendrites are prone to form under high current densities, our full batteries have been proved to possess very promising performance, particularly, the rate capability for the practical applications (Table S5, Supporting Information).

3. Conclusion

To conclude, P (V) in argyrodite LPSI electrolyte was partially replaced by Sn (IV) to form a series of new LPSI-*x*Sn electrolytes. The larger cell volume and increased Li^+ solubility resulting from Sn substitution for P in the PS_4 tetrahedral structure endow the optimized LPSI-20Sn electrolyte with two orders of magnitudes higher (125 times) ionic conductivity (3.5×10^{-4} S cm^{-1}) compared with LPSI electrolyte (2.8×10^{-6} S cm^{-1}). More remarkably, the optimized LPSI-20Sn electrolyte is also proved to possess excellent air stability (O_2 and moisture) derived from the strong Sn–S bonding energy in $(P/Sn)S_4$ structure. The mass and ionic conductivity of LPSI-20Sn exhibits negligible changes after O_2 and 10% humidity exposure (after reheating), respectively. In addition, benefiting from the I-based chemistry in stabilizing the Li metal anode interface against sulfide electrolytes, Li–Li symmetric cells using LPSI-20Sn as the electrolyte can exhibit outstanding plating and stripping for over 200 h at a high current density (1.26 mA cm^{-2}) and cut-off capacity (1 mAh cm^{-2}) in the Li//LPSI-20Sn//Li symmetric cell. LPSI-20Sn electrolyte was further employed as the Li metal anode interlayer in ASSLMBs to provide a stabilized Li metal anode interface for achieving excellent cycling stability and rate capability. All these results suggest that the reasonable aliovalent element substitution for the problematic element in promising sulfide electrolytes can exhibit multifunction capabilities and make them more suitable for application in sulfide-based ASSLMBs.

4. Experimental Section

Materials: All materials were used directly without any purification. P_2S_5 (>99%), LiI (99.99%, anhydrous), LiCl (>99.98%, anhydrous), LiBr (99.9%, anhydrous), and LCO (99.8%) particles were purchased from Sigma-Aldrich. Li_2S (99.9%) was purchased from Alfa Aesar. SnS_2 (99.999%) was purchased from American Elements.

Preparation of LPSI-xSn Sulfide SSEs (x, the Sn Substitution Percentage, Equals to 0, 10, 15, 17.5, 20, 22.5, 25, 30, 50, 80, and 100): Stoichiometric raw materials (Li_2S, P_2S_5, LiI, and SnS_2) were weighed (total 1 g) and sealed in zirconia ball milling pots. The mass ratio between the mixture and the zirconia ball was 1:40. Low-speed ball milling (180 rpm for 2 h) was used at first to fully mix the starting materials. After that, high-speed of 510 rpm for 13 h was conducted on the mixture. All ball milling processes were protected under Ar gas atmosphere by using planetary ball milling apparatus. Then, the ball-milled product was pressed into pellets, and sealed in quartz tubes for postannealing treatment. The annealing condition was 450 °C/8 h in the muffle furnace. The rate of increasing temperature was fixed at 5 °C min^{-1}. After the annealing was completed, the sample naturally cooled down to RT. It was noted that S vacancy can be produced by partly replacing P_2S_5 with SnS_2 in the starting raw materials, which can be represented by the following defect equation using Kröger–Vink notation: $2SnS_2 \xrightarrow{P_2S_5} 2Sn_P^{\prime} + 4S_S^{\times} + V_S^{\bullet\bullet}$. Through reacting with other reactants, the S vacancy was occupied, while more Li atoms were introduced to keep the charge balance, increasing the solubility of Li^+ ions in the crystal structure.

Preparation of LPSBr-xSn SSEs (Substitution Percentage x = 1, 2.5, 5, 10, 12.5, 15, 20, 30) and LPSCl-xSn SSEs (Substitution Percentage x = 0 and 30): Li_2S, P_2S_5, SnS_2, and LiBr were used for LPSBr-*x*Sn SSEs preparation, while Li_2S, P_2S_5, SnS_2, and LiCl raw materials for LPSCl-*x*Sn. Similar to the preparation process of synthesizing LPSI-*x*Sn SSEs, same ball milling condition and annealing process were used to prepare LPSBr-*x*Sn and LPSCl-*x*Sn SSEs.

Preparation of LCO@LNO Cathode Materials and LCO@LNO/LGPS Cathode Composites: According to the previously reported method from the group,[28] ALD process was used to prepare a $LiNbO_x$ coating layer on the commercial LCO particles to form LCO@LNO composites. The LCO@LNO/LGPS cathode composite was prepared by milling LCO@LNO powder and LGPS electrolyte (mass ratio 7:3) with a roll mixer.

Ionic Conductivity Measurements: Ionic conductivity of prepared SSEs was measured by the EIS measurements and corresponding simulation method. EIS measurements were completed on a multichannel potentiostation 3/Z (German VMP3). The applied frequency range was 0.1 Hz to 7 MHz and the amplitude was 20 mV. The test cell was fabricated as follows: 80 mg of the SSEs were pressed into a pellet (diameter 1 cm, thickness 0.7 mm) with a pressure of ≈300 MPa. Subsequently, two pieces of indium (In) foil serving as the current collector were pressed on both sides of the electrolyte pellet in a model cell. To gain the Arrhenius plot, variable-temperature EIS was measured from −5 to 45 °C with an interval of 10 °C.

Cell Assembly and Electrochemical Measurements: For Li//LPSI-20Sn//Li symmetric cells, typically, 80 mg of LPSI-20Sn electrolyte was pressed by ≈300 MPa to form solid pellet. Two pieces of Li metal (China Energy Lithium Co., Ltd.) were placed onto both sides of the LPSI-20Sn pellet and then pressed by ≈120 MPa for 3 min. Li plating/stripping experiments were carried out on LAND battery testing stations (CT-2001A, Wuhan Rambo Testing Equipment Co., Ltd.). Current density and cut-off capacity were set at 0.1 mA cm^{-2} and 0.1 mAh cm^{-2}. Li/LPSI-20Sn//LGPS//LCO@LNO//LGPS ASSLMBs were fabricated using LGPS as the electrolyte, prepared LCO@LNO/LGPS as the cathode composite, LPSI-20Sn as the Li metal anode interlayer, and Li metal as the anode. Typically, 80 mg of the LGPS electrolyte (purchased from MSE supplies LLC) was pressed under ≈300 MPa to form a solid LGPS layer (diameter: 10 mm, thickness: 0.65 mm). 20 mg of LPSI-20Sn electrolyte was spread on one side of the LGPS layer, and pressed under ≈300 MPa to form an interlayer (diameter: 10 mm, thickness: 0.17 mm) to separate Li metal and LGPS layer. 10 mg of LCO@LNO/LGPS powder was uniformly spread onto the surface of the other side of LGPS layer and pressed under ≈360 MPa for 5 min. Finally, Li metal was placed on the LPSI-20Sn layer and pressed by ≈120 MPa for 3 min. The four-layered pellet cell was sandwiched between two stainless-steel rods as current collectors and sealed in the model cell. Galvanostatic charge–discharge was conducted on the LAND battery test system. The voltage window was set as 2.8–4.2 V (vs Li/Li^+), and various constant current densities were applied to evaluate the cycling stability and the rate performance. All cell fabrication processes were conducted in an Ar-filled glovebox.

Air Stability Measurements: The electrolyte stability against dry O_2 was measured in the TGA instrument. Powder electrolytes were placed in the atmosphere of continuous flow of dry O_2 with the weight recorded by the built-in microbalance. The stability toward moisture was evaluated as follows: electrolytes were placed in an airtight chamber with humidity and gas (O_2, N_2, air, and vacuum) controlling. After exposure of 10% humidity overnight, XRD and the EIS measurements were conducted for the electrolyte samples. Reheating process was processed in a vacuum oven (180 °C) overnight.

© 2020 WILEY-VCH Verlag GmbH & Co. KGaA, Weinheim

Characterization: SEM images and element mapping were obtained by using a Hitachi S-4800 field-emission scanning electron microscope (FE-SEM, acceleration voltage 5 kV) equipped with EDS. XRD measurements were performed on Bruker AXS D8 Advance with Cu Kα radiation (λ = 1.54178 Å). Kapton tape was covered on the XRD holder to prevent from the air exposure. Low-speed-scan XRD pattern of LPSI-20Sn electrolyte was obtained by scanning at the speed of 5 s per step (1 step = 0.02°) from 10° to 90° (2θ). XRD Rietveld refinement was performed by using Materials Studio software. Raman spectra were measured with a HORIBA Scientific LabRAM HR Raman spectrometer operated under an incident laser beam at 532 nm. Electrolyte samples were sealed and sandwiched in two pieces of transparent glasses for Raman testing. XPS spectra were obtained by using Krotos AXIS Ultra Spectrometer system using a monochromatic Al K(alpha) source (25 mA, 15 kV). Solid-state ^{7}Li NMR measurements were carried out on a Varian Infinity Plus 400 (I+400) NMR spectrometer (B_o = 9.4 T), operating at a ^{7}Li resonance frequency of 155.248 MHz. The $\pi/2$ pulse length was determined to be 2.3 µs. Chemical shifts were referenced with respect to a 1.0 M LiCl solution. The electrolyte sample was sealed in custom-made Teflon tubes (ϕ = 4.7 mm) in an argon-filled glovebox. Variable temperature (–40 to 130 °C with an interval of 5 or 10 °C) measurements were performed by using a 5 mm static probe. T_1 relaxation (spin–lattice) time at various temperatures was determined by using the saturation recovery method.

DFT Calculation: It was conducted for both static computation and geometry optimization of LPSI and LPSI-20Sn crystal, using the CASTEP DFT code of Accelrys Material Studio 8.0 with the exchange–correlation functional of Perdew–Burke–Ernzerhof (PBE) based on the generalized gradient approximation (GGA).[29] The cut-off energy for the plane-wave basis was set as 380.0 eV. The *k*-point mesh of 2 × 2 × 2 was adopted and the self-consistent field tolerance was set as 5.0×10^{-7} eV Å^{-1}. The fast Fourier transform grid density was set as 90 × 90 × 90. The crystal structure of LPSI-20Sn crystal was employed by using different occupation ratios of Sn and P in the same site position. The oxygen replacement reaction energy (ΔE) of LPSI-20Sn and LPSI electrolytes was simulated based on the differential energy by changing one of the S atoms to O atom in the model structure. One 2 × 2 × 2 supercell of LPSI or LPSI-20Sn was used as the model structure by changing one of the S atoms. The oxygen replacement reaction energy (ΔE) can be calculated as $\Delta E = U_{(\text{S atom})} + U_{(\text{PS3O tetrahedron})} - U_{(\text{O atom})} - U_{(\text{PS4 tetrahedron})}$, which can be defined as one of the indicators to reveal the resistance capability of sulfide electrolyte (containing PS_4 tetrahedron) to O_2.

Supporting Information

Supporting Information is available from the Wiley Online Library or from the author.

Acknowledgements

F.Z. and J.L. contributed equally to this work. This research was supported by the Natural Sciences and Engineering Research Council of Canada (NSERC), the Canada Research Chair Program (CRC), the Canada Foundation for Innovation (CFI), Ontario Research Foundation (ORF), China Automotive Battery Research Institute Co., Ltd., Glabat Solid-State Battery Inc., and the University of Western Ontario (UWO).

Conflict of Interest

The authors declare no conflict of interest.

Keywords

air stability, all-solid-state Li metal batteries, argyrodite sulfide, Li metal compatibility, Sn (IV) substitution

Received: October 18, 2019
Revised: December 16, 2019
Published online:

[1] a) A. Manthiram, X. Yu, S. Wang, *Nat. Rev. Mater.* **2017**, *2*, 16103; b) Y. Kato, S. Hori, T. Saito, K. Suzuki, M. Hirayama, A. Mitsui, M. Yonemura, H. Iba, R. Kanno, *Nat. Energy* **2016**, *1*, 16030; c) N. Kamaya, K. Homma, Y. Yamakawa, M. Hirayama, R. Kanno, M. Yonemura, T. Kamiyama, Y. Kato, S. Hama, K. Kawamoto, A. Mitsui, *Nat. Mater.* **2011**, *10*, 682.

[2] a) Z. Zhang, Y. Shao, B. Lotsch, Y.-S. Hu, H. Li, J. Janek, L. F. Nazar, C.-W. Nan, J. Maier, M. Armand, L. Chen, *Energy Environ. Sci.* **2018**, *11*, 1945; b) Z. Gao, H. Sun, L. Fu, F. Ye, Y. Zhang, W. Luo, Y. Huang, *Adv. Mater.* **2018**, *30*, 1705702.

[3] a) S. Chen, D. Xie, G. Liu, J. P. Mwizerwa, Q. Zhang, Y. Zhao, X. Xu, X. Yao, *Energy Storage Mater.* **2018**, *14*, 58; b) J. Lau, R. H. DeBlock, D. M. Butts, D. S. Ashby, C. S. Choi, B. S. Dunn, *Adv. Energy Mater.* **2018**, *8*, 1800933.

[4] a) S. P. Culver, R. Koerver, T. Krauskopf, W. G. Zeier, *Chem. Mater.* **2018**, *30*, 4179; b) R. C. Xu, X. H. Xia, S. Z. Zhang, D. Xie, X. L. Wang, J. P. Tu, *Electrochim. Acta* **2018**, *284*, 177.

[5] a) L. Fan, S. Wei, S. Li, Q. Li, Y. Lu, *Adv. Energy Mater.* **2018**, *8*, 1702657; b) P. Albertus, S. Babinec, S. Litzelman, A. Newman, *Nat. Energy* **2018**, *3*, 16; c) Y. Zhu, X. He, Y. Mo, *ACS Appl. Mater. Interfaces* **2015**, *7*, 23685.

[6] A. Kato, H. Kowada, M. Deguchi, C. Hotehama, A. Hayashi, M. Tatsumisago, *Solid State Ionics* **2018**, *322*, 1.

[7] S. Wenzel, D. A. Weber, T. Leichtweiss, M. R. Busche, J. Sann, J. Janek, *Solid State Ionics* **2016**, *286*, 24.

[8] S. Wenzel, S. J. Sedlmaier, C. Dietrich, W. G. Zeier, J. Janek, *Solid State Ionics* **2018**, *318*, 102.

[9] S. Wenzel, S. Randau, T. Leichtweiß, D. A. Weber, J. Sann, W. G. Zeier, J. Janek, *Chem. Mater.* **2016**, *28*, 2400.

[10] a) M. Nagao, A. Hayashi, M. Tatsumisago, T. Kanetsuku, T. Tsuda, S. Kuwabata, *Phys. Chem. Chem. Phys.* **2013**, *15*, 18600; b) X. B. Cheng, R. Zhang, C. Z. Zhao, Q. Zhang, *Chem. Rev.* **2017**, *117*, 10403.

[11] a) H. Muramatsu, A. Hayashi, T. Ohtomo, S. Hama, M. Tatsumisago, *Solid State Ionics* **2011**, *182*, 116; b) G. W. Luther, A. J. Findlay, D. J. Macdonald, S. M. Owings, T. E. Hanson, R. A. Beinart, P. R. Girguis, *Front. Microbiol.* **2011**, *2*, 62.

[12] a) Y. Gao, D. W. Wang, Y. G. C. Li, Z. X. Yu, T. E. Mallouk, D. H. Wang, *Angew. Chem., Int. Ed.* **2018**, *57*, 13608; b) R. Xu, F. Han, X. Ji, X. Fan, J. Tu, C. Wang, *Nano Energy* **2018**, *53*, 958; c) X. L. Fan, X. Ji, F. D. Han, J. Yue, J. Chen, L. Chen, T. Deng, J. J. Jiang, C. S. Wang, *Sci. Adv.* **2018**, *4*, eaau9245; d) F. D. Han, J. Yue, X. Zhu, C. S. Wang, *Adv. Energy Mater.* **2018**, *8*, 1703644.

[13] M. Suyama, A. Kato, A. Sakuda, A. Hayashi, M. Tatsumisago, *Electrochim. Acta* **2018**, *286*, 158.

[14] a) J. A. Brant, D. M. Massi, N. A. W. Holzwarth, J. H. MacNeil, A. P. Douvalis, T. Bakas, S. W. Martin, M. D. Gross, J. A. Aitken, *Chem. Mater.* **2015**, *27*, 189; b) T. Kaib, S. Haddadpour, M. Kapitein, P. Bron, C. Schröder, H. Eckert, B. Roling, S. Dehnen, *Chem. Mater.* **2012**, *24*, 2211; c) K. Kanazawa, S. Yubuchi, C. Hotehama, M. Otoyama, S. Shimono, H. Ishibashi, Y. Kubota, A. Sakuda, A. Hayashi, M. Tatsumisago, *Inorg. Chem.* **2018**, *57*, 9925.

[15] G. Sahu, Z. Lin, J. Li, Z. Liu, N. Dudney, C. Liang, *Energy Environ. Sci.* **2014**, *7*, 1053.

 © 2020 WILEY-VCH Verlag GmbH & Co. KGaA, Weinheim

[16] a) M. A. Kraft, S. Ohno, T. Zinkevich, R. Koerver, S. P. Culver, T. Fuchs, A. Senyshyn, S. Indris, B. J. Morgan, W. G. Zeier, *J. Am. Chem. Soc.* **2018**, *140*, 16330; b) N. Minafra, S. P. Culver, T. Krauskopf, A. Senyshyn, W. G. Zeier, *J. Mater. Chem. A* **2018**, *6*, 645.
[17] a) H. J. Deiseroth, S. T. Kong, H. Eckert, J. Vannahme, C. Reiner, T. Zaiss, M. Schlosser, *Angew. Chem., Int. Ed.* **2008**, *47*, 755; b) C. Yu, L. van Eijck, S. Ganapathy, M. Wagemaker, *Electrochim. Acta* **2016**, *215*, 93; c) C. Yu, S. Ganapathy, J. Hageman, L. van Eijck, E. R. H. van Eck, L. Zhang, T. Schwietert, S. Basak, E. M. Kelder, M. Wagemaker, *ACS Appl. Mater. Interfaces* **2018**, *10*, 33296.
[18] Z. Zhang, L. Zhang, X. Yan, H. Wang, Y. Liu, C. Yu, X. Cao, L. van Eijck, B. Wen, *J. Power Sources* **2019**, *410–411*, 162.
[19] M. A. Kraft, S. P. Culver, M. Calderon, F. Bocher, T. Krauskopf, A. Senyshyn, C. Dietrich, A. Zevalkink, J. Janek, W. G. Zeier, *J. Am. Chem. Soc.* **2017**, *139*, 10909.
[20] S. Ohno, B. Helm, T. Fuchs, G. Dewald, M. A. Kraft, S. P. Culver, A. Senyshyn, W. G. Zeier, *Chem. Mater.* **2019**, *31*, 4936.
[21] S. Yubuchi, S. Teragawa, K. Aso, K. Tadanaga, A. Hayashi, M. Tatsumisago, *J. Power Sources* **2015**, *293*, 941.
[22] C. Yu, S. Ganapathy, N. J. J. de Klerk, I. Roslon, E. R. H. van Eck, A. P. M. Kentgens, M. Wagemaker, *J. Am. Chem. Soc.* **2016**, *138*, 11192.
[23] S. Ganapathy, C. Yu, E. R. H. van Eck, M. Wagemaker, *ACS Energy Lett.* **2019**, *4*, 1092.
[24] S. Kim, S. K. Kim, P. C. Sun, N. Oh, P. V. Braun, *Nano Lett.* **2017**, *17*, 6893.
[25] Y. Lu, Z. Tu, L. A. Archer, *Nat. Mater.* **2014**, *13*, 961.
[26] K. Mizushima, P. C. Jones, P. J. Wiseman, J. B. Goodenough, *Mater. Res. Bull.* **1980**, *15*, 783.
[27] C. Yu, S. Ganapathy, E. Eck, H. Wang, S. Basak, Z. Li, M. Wagemaker, *Nat. Commun.* **2017**, *8*, 1086.
[28] B. Wang, Y. Zhao, M. N. Banis, Q. Sun, K. R. Adair, R. Li, T. K. Sham, X. Sun, *ACS Appl. Mater. Interfaces* **2018**, *10*, 1654.
[29] a) M. D. Segall, P. J. D. Lindan, M. J. Probert, C. J. Pickard, P. J. Hasnip, S. J. Clark, M. C. Payne, *J. Phys.: Condens. Matter* **2002**, *14*, 2717; b) S. J. Clark, M. D. Segall, C. J. Pickard, P. J. Hasnip, M. J. Probert, K. Refson, M. C. Payne, *Z. Kristallogr.* **2005**, *220*, 567.

© 2020 WILEY-VCH Verlag GmbH & Co. KGaA, Weinheim